Asteroid Origins Satellite (AOSAT) I: An On-orbit Centrifuge Science Laboratory

Jack Lightholder*, Andrew Thoesen*, Eric Adamson, Jeremy Jakubowski,
Ravi Nallapu, Sarah Smallwood, Laksh Raura, Andrew Klesh,
Erik Asphaug, Jekan Thangavelautham

Arizona State University, Tempe, AZ 85287

Abstract

Exploration of asteroids, comets and small moons ('small bodies') can answer fundamental questions relating to the formation of the solar system, the availability of resources, and the nature of impact hazards. Near-earth asteroids and the small moons of Mars are potential targets of human exploration. But as illustrated by recent missions, small body surface exploration remains challenging, expensive, and fraught with risk. Despite their small size, they are among the most extreme planetary environments, with low and irregular gravity, loosely-bound regolith, extreme temperature variation, and the presence of electrically charged dust. Here we describe the Asteroid Origins Satellite (AOSAT-I), an on-orbit, 3U CubeSat centrifuge using a sandwich-sized bed of crushed meteorite fragments to replicate asteroid surface conditions. Demonstration of this CubeSat will provide a low-cost pathway to physical asteroid model validation, shed light on the origin and geophysics of asteroids, and constrain the design of future landers, rovers, resource extractors, and human missions. AOSAT-I will conduct scientific experiments within its payload chamber while operating in two distinct modes: 1) as a nonrotating microgravity laboratory to investigate primary accretion, and 2) as a rotating centrifuge producing artificial milligravity to simulate surface conditions on asteroids, comets and small moons. AOSAT-I takes advantage of low-cost, off-the-shelf components, modular design, and the rapid assembly and instrumentation of the CubeSat standard, to answer fundamental questions in planetary science and reduce cost and risk of future exploration.

Keywords: CubeSat, Centrifuge, Asteroids, Laboratory

1. Introduction

Spacecraft missions to asteroids, comets and small moons are driving advances toward answering fundamental questions regarding the physics and chemistry of solar system formation, and the origins of organic molecules, the building blocks of life. Geophysical studies of cratering and dynamical processes on near-Earth asteroids improve collision mitigation efforts that safeguard the Earth. Addressing these and other important questions requires exploration and in situ sampling from the surfaces and interiors of small bodies, as called out in the NRC Decadal Survey [1]. However, surface exploration of comets, moons and asteroids is a daunting challenge, as evidenced by the Hayabusa [2], Philae [3], Phobos [4] and NEAR [5] missions and the difficulties they faced. Today there are two missions in cruise phase to small asteroids, the Hayabusa-2 mission and the OSIRIS-REx mission, both to perform touch and go sampling operations.

Hayabusa-2 will include several surface science experiments including the firing of a 2-kg projectile at 2 km/s to make a several-meter crater [6]. The era of landed investigations on asteroids will commence when Hayabusa-2 deploys the DLR MASCOT lander [7] and the Minerva-2 small robotic payloads [8]. Designing for surface operations is deeply challenged by the wide range of operational conditions possible with the largely unknown surface properties. Proposed flagship investigations like the Asteroid Retrieval Mission (ARM) rely on some understanding of the mechanical behaviors and geologic structural conditions to be expected in milligravity, that is, gravitational accelerations around 1/1000 that of Earth. Are the surfaces of small bodies rigid, or as soft and fluid as quicksand? These and other questions must be answered in order to develop refined models and low-risk operational strategies. Additionally, for most asteroids and other small bodies of interest, in addition to milligravity their surfaces consist of fine debris and coarse debris, possibly a global 'rubble pile' constitution, and diurnal cycles of hours with associated extreme changes in temperature. The environment can be highly dynamic, and much more alien than the Moon. Grappling or anchoring onto the surface of a small body presents a major challenge. The development of relevant technologies, enabling successful asteroid landings, as well as extending surface exploration missions, requires the refinement of our existing physical models of the relevant surface and near-surface environments, which, in turn, will guide the design and development of next generation landers.

Missions to asteroids and comets remain expensive, long duration endeavors, fraught with high-risk. A credible risk mitigation step is to recreate asteroid and comet environments inside a laboratory. It is feasible to generate low-gravity environments on Earth, for instance, by using buoyancy methods, air tables, drop towers and parabolic flights. While missions like BORE (Box of Rocks Experiment) do exist[9], these methods have important limitations. Low-gravity phenomena may be simulated by submersion in fluids, but the reduction of the earth's gravitational attraction is limited to the magnitude of buoyancy. Air tables may be used to simulate low gravity conditions, but this method confines interactions to two-dimensions. ISS posseses a small centrifuge system that focuses on Biology and Microbiology experiments ranging from micro-g to 1-g. Additionally, drop towers and parabolic flights produce very low gravity environments; however these are only for short timescales of 5-15 seconds. All of these options are limited, either not sufficiently representative of asteroid surface physics, or else just a brief window into that environment.

A credible alternative for long-term laboratory research of small bodies is to simulate milligravity geological conditions inside a centrifuge laboratory in Low Earth Orbit (LEO). As noted in Section 2, proposals for centrifuges in space are not new (see for instance, [10, 11]). However, previous centrifuge concepts were designed for human habitats or manufacturing and processing, often consisting of a rotating spacecraft, connected to a stationary one. Such a design poses significant challenges [12] as it requires the imposition of a counter-spin to ensure parts of the spacecraft remain stationary, thus requiring large, custom-designed, persistent reaction wheels. At the other extreme, a small sample-separation centrifuge to spin test-tubes to high-g has been installed by Nanoracks onboard the ISS. Accessing the middle-ground of low-but-nonzero gravity has so far not been possible.

We propose a simplified centrifuge laboratory for simulating small bodies such as asteroids using a low-cost 3U CubeSat [13, 14]. The entire 3U spacecraft is designed to spin about its system chamber while carrying a large payload chamber containing crushed meteorites (regolith), which are the remnants of asteroids. A centrifuge spinning at low angular velocity will simulate the gravity expected on these small bodies. The advantage of this approach is that it enables the simulation of asteroid and comet surface conditions without requiring the mission costs associated with in situ exploration of such interesting bodies. This laboratory will facilitate the development and testing of new technologies offering rapid turn-around time for relatively

low cost.

Herein, we present a detailed discussion of the design and instrumentation of AOSAT I, which will be the first space centrifuge for studying milligravity environments. Our current work focuses on investigating the concept feasibility, system design, deployment mechanism and power requirements of launching and operating a 3U (3000 cm^3) CubeSat centrifuge system in orbit. The spacecraft includes a 2U experimental chamber containing regolith, enabling scientific experiments within its payload chamber while operating in two distinct modes: 1) a centrifuge producing artificial gravity to simulate surface conditions on asteroids of < 1 km diameter, and 2) as a stationary microgravity laboratory to investigate primary accretion. These experiments will advance knowledge of planet formation and surface properties of asteroids. Within the payload are several instruments including a camera array, lights, shaker platform and a bead deployer (for investigating impact dynamics). The remaining 1U partition contains the spacecraft computer, communications systems, and attitude determination and control system. Major design challenges related to spacecraft stability must be overcome due to the shifting regolith within the relatively large experimental chamber. The proposed system illustrates the effective use of low-cost, off-the-shelf components in the rapid assembly and instrumentation of a CubeSat science laboratory. Demonstration of this CubeSat will provide a low-cost pathway to physical asteroid physics model validation, shed light on asteroid origins, and constrain the design of future asteroid surface probes.

In Section 2 we present background on particle aggregation physics in microgravity, as well as the use of centrifuges to produce "artificial gravity", followed by a detailed discussion of the design of AOSAT I in Section 3. Section 4 describes physical and numerical models that were employed to constrain the system design and to analyze operation of critical mechanisms. The implications of these results on overall system performance are discussed in detail within Section 5 and conclusion are summarized in Section 6.

2. Background

The scientific goals of the AOSAT I mission are two-fold: 1) investigate the process of particle coagulation in microgravity (close to zero-g), and 2) model the near-surface milligravity ($\sim 10^{-3}$ g$_\oplus \sim 1$ cm s^{-2}) characteristics of small asteroids, where g$_\oplus$ is Earth gravity. In addition to performing groundbreaking asteroid science, the successful demonstration of this first on-orbit

spacecraft centrifuge will enable advanced future missions that will further illuminate fundamental aspects of the early formation of planetary bodies, and will provide detailed experimentally-derived knowledge of the physical properties of asteroid surface and sub-surface environments and operations therein.

2.1. Particle Aggregation

Planets are formed in protoplanetary disks as a result of star formation. Within protoplanetary disks, dust coalesces to planetesimals, a vital step in the planet formation process. However, this coalescence process is not well understood [15]. Multiple hypotheses exist regarding the relevant parameters which may lead to particle aggregation in space, and this has been assessed in various ways. Brisset et al. [16] studied dust aggregate collision behavior on the suborbital rocket flight REXUS 12 to further understand the mechanisms behind the first phase of planet formation. Onboard the International Space Station, Love et al. [17] investigated particle aggregation of various types and sizes of angular sub-millimeter particulate. Marshall et al. [18] preferentially chose sub-millimeter quartz and volcanic ash particulate to fly in microgravity aboard Space Shuttle Columbia in a chamber environment (ensuring particle suspension) in order to observe coagulation. Dust synthesis and modeling has been done in laboratory conditions in order to understand the morphology of grain growth to constrain future models of primary planetary accretion by Praburam and Goree [19].

We propose to directly observe granular coagulation processes for periods of up to 15 hours within the AOSAT I microgravity laboratory. We will image the regolith in zero-gravity, while the spacecraft is not spinning, and then apply the spacecraft flywheel torque to mobilize and gather the material, in a series of experiments that can be compared with and validate model prediction. A single science chamber of 19.2 cm will be utilized within AOSAT I. The science chamber will contain ~ 0.3 kg of Tamdakht meteorite material [20] an H5 ordinary chondrite, with a range of particle sizes approximately fitting a cumulative size distribution $n(d) \propto d^{-3}$. For AOSAT-I these particles will be sieved to mm-sizes to avoid the complexities associated with imaging a dust-laden experiment, focusing on the granular physics of the coagulation process.

2.2. Asteroid Surface Geophysics

The primary, novel experiments of AOSAT-I will be to study asteroid surface geophysics, as it will be the first space centrifuge for studying milligravity environments. These experiments are fundamentally to watch what happens when various forces (rotations and vibrations) are applied to a bed of airless meteorite regolith particles, forces that will be closely analogous to those representative of the surface conditions of small asteroids.

The concept of utilizing rotational motion to simulate gravitational acceleration in space was first proposed by Konstantin Tsiolkovsky just prior to the turn of the 20th century [21]. A thorough investigation of the details related to such a space based centrifuge apparatus was presented by Theodore Hall in his doctoral dissertation [22]. Though this concept has seen great popularity in science fiction since its inception, spaceborne experiments have been sparse. The first occurred during the Gemini 11 mission in 1966 [23]. This experiment required tethering the Gemini 11 spacecraft to its Agena Target Vehicle by a 30 m tether and initiating a rotation of approximately 0.15 revs/min. The resulting artificial gravity is estimated to have been approximately 1.5×10^{-4} $\mathbf{g}$ (where $\mathbf{g} = 9.81$ m/s^2 is the gravitational acceleration at the surface of the earth). Neither astronaut on board the spacecraft was able to detect such a small force, however, the astronauts observed a camera resting on the instrument panel to accelerate toward the outer wall of the craft, parallel to the tether.

Since the Gemini 11 mission, significant work has focused on Tethered Satellite Systems (TSS) (for detailed reviews see [24], [25] and [26]), from relatively simple two-body dumbbell configurations, conceptually similar to the Gemini 11 experiment, to triangular [27], wheel-and-spoke [28] and more complicated configurations consisting of numerous spacecraft. Such TSSs offer great potential for space research focusing on the generation of electricity, artificial gravity, and upper atmospheric research. However, these systems also pose significant challenges, particularly in terms of spacecraft stability.

Centrifuge concepts from 1950s and 1960s generated numerous proposals for spinning space colonies (Figure 1). More practical attempts at developing centrifuges include the Centrifuge Accommodation Module (CAM), developed by the Japanese Aerospace Exploration Agency (JAXA) and which was to be operated by NASA. The CAM was intended to be used to conduct various biological and life-science related experiments, providing between 0.01 $\mathbf{g}$ to 2 $\mathbf{g}$ [29, 30]. It is significant to note that this chamber would

6

have facilitated operation at two distinct values of artificial gravity (i.e., angular velocity). A more ambitious centrifuge concept was proposed from NASA's Johnson Space Center (JSC) in 2011 [31], consisting of an inflatable centrifuge attached to the International Space Station (ISS). The attached centrifuge would have provided the sleeping module for the ISS crew. This centrifuge was intended to be a low-cost demonstration for a multi-mission manned space exploration vehicle, NAUTILUS-X, that would be placed at L1 and operate as a staging ground/living quarters for subsequent missions to Mars and beyond. Small-scale centrifuges have also been developed for applications focusing on microbiology research in space at the cellular/molecular level [32]. In 2004, we proposed the development CubeSat-sized centrifuges in space to simulate milligravity conditions to 1 **g** for a range of applications including planetary science to life science and in-space manufacturing [13, 14].
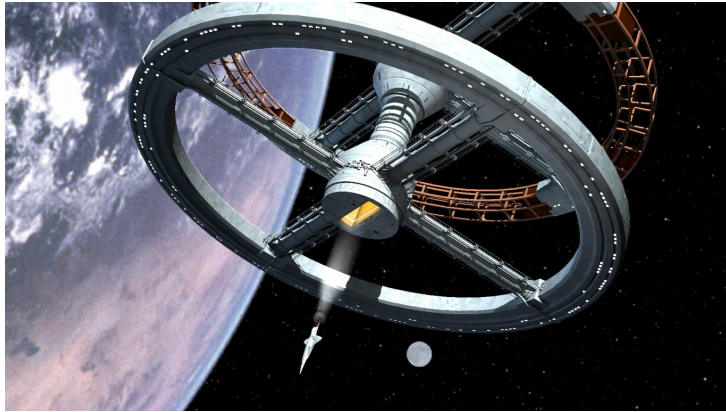

Figure 1: Artist Concept of a Spinning Space Colony (courtesy of Mark Tims).

AOSAT-I is the first spacecraft centrifuge for studying milligravity environments, and in fact will be the first whole-spacecraft research centrifuge. It achieves this goal by looking at small gravitational forces common to an asteroid, which are typically 1/1000 that of Earth. If one sets the centripetal acceleration $r\omega^2$ equal to the gravitational acceleration GM/R^2 where r is the radius of the centrifuge (approx. 17 cm for AOSAT-I, from the center of mass to the center of the regolith bed) and where M and R are the mass and radius of a spherical, non-rotating asteroid of uniform density ρ (there are no such things, but this is an approximation), then $\omega = \sqrt{4/3\pi G\rho R/r}$. Measuring ω in rpm (revolutions per minute) and R in km, and assuming

$\rho = 2$ g cm^{-3} one obtains the approximation $\omega_{rpm} = 0.55\sqrt{R_{km}}$. Therefore spacecraft rotations with an order of magnitude of 1 rpm is perfect for studying asteroid surface gravity conditions, for bodies 0.1 to 10 km in radius (e.g. small-NEO to Phobos-sized). There is no lower limit to ω, but we consider 4 rpm to be a safe upper limit. Stability at higher rpm will be evaluated in flight, at the end of mission.

AOSAT-I is designed to obtain stable CubeSat rotations of 0-4 rpm using a flywheel for the primary spin axis, stabilized by magnetically induced torques. These are slow rotations, but as we shall see one of the challenges in designing AOSAT I is to prove that this is a stable experimental configuration, within the tolerances of the experiment. We note therefore that absolute, constant asteroid-like gravity conditions are not the requirement. After all, the centripetal acceleration some distance closer to the spin axis, will be lower than the acceleration at the 'bottom' of the lab chamber, so we cannot achieve constant gravity. Moreover, any nutation of the spacecraft during its rotation will cause the regolith bed to feel accelerations to the left and right, per rotation. While these irregularities must be guarded against, primarily to prevent destabilization of the spacecraft (tumbling), they are not problematic from the point of view of the milligravity experimentation, since part of the study is to understand the stability of asteroid land-forms to various kinds of stresses, and this would be an oscillatory stress.

All of these data will be used to validate high definition simulations of granular physics on and beneath the surfaces of small planetary bodies – whose gravity itself is irregular, and oscillatory. A typical small NEO spins with a period as fast as a few hours, or faster, and can have surface (effective) gravity varying by a factor of 2-3 from location to location, and changing considerably with depth. So nutations and other sources of acceleration inside of the AOSAT-I lab chamber need to be monitored and understood and tracked, for modeling purposes, but do not need to be eliminated.

3. System Design

3.1. Concept of Operations

The system is centered around an experiment consisting of 300 g of meteorite fragments, that are subjected to various external and internal forces: spacecraft rotations, tunable vibrations, and various forms of inter-particulate and particle-spacecraft cohesion. The supporting infrastructure of AOSAT-I is designed to observe the behavior of this material, providing

a flat and measured chamber (to facilitate observation and interpretation), banks of LEDs for variable kinds of illumination, tunable buzzers, and stereo cameras.

The regolith is produced by pounding and crushing pieces of the H5 ordinary chondrite meteorite Tamdakht, sieved into a cumulative size distribution with exponent -2 to -3 and a smallest grain diameter 2 mm, and then sealed behind the launch-door of the payload chamber. The meteorite fragments are produced in other experiments (strength-to failure; ballistics) and are selected from an interior fragment of Tamdakht, approx. 9 kg total mass, that was never subject to atmospheric stresses or thermal heating upon Earth impact (no fusion crust). Fragments of Tamdakht have strength and hardness characteristics similar to concrete [33]. The fragments are stored carefully, and after sieving are rinsed in methanol to remove any possible handling residues and to detach any sub-mm particulates; then they are dried under vacuum conditions prior to payload integration. (The engineering model of the AOSAT-I lab chamber uses fragments of concrete, with comparable strength and hardness, instead of meteorite.)

During the science phases, this asteroid-regolith payload will freely float in a rectangular payload chamber 8.3 cm × 8.3 cm × 19.2 cm. Stereo cameras and banks of LEDs will be used to resolve discrete grains and image aggregate particulate behavior. But the granular payload must be confined during lift-off, otherwise crushing vibrations and shaking would damage the grains and introduce dust to the lab chamber. The stored behind a door during launch, to be opened once zero-g is established. The opening of this door begins the science investigation, and the initial release of particles constitutes the first experiment.

Science operations consist of two phases: (1) release of regolith and tracking of particles in the non-rotating spacecraft, to study aggregation of particles to each other or to the walls; and (2) centrifuge experiments in a rotating spacecraft mimicking asteroid surface conditions, to study regolith settling and granular stability and aggregate behavior/flow.

3.1.1. Science Phase 1

The first phase begins when a single door mechanism (shown in Figure 3) is deployed to release the regolith. A nichrome burn-wire door-release mechanism is activated, allowing the door to come to a position flush with the inner wall of the payload. By this time the fragments will have mostly equilibrated to vacuum from the 1 bar payload environment, but might un-

dergo some final dehydration and degassing especially once released from dense packing behind the door. Particle behavior will be analyzed twice, once as they tumble out of the door, and then 7 days later to observe their freely-floating configuration, to see if there are any changes related to particle equilibration.

Regolith aggregation will be monitored in the first stage using stereo cameras, during and after door deployment, and then in an experiment applying the buzzer to look for standing patterns forming in zero-gravity. Particle aggregation will be auto-detected on the basis of Shannon's entropy of the image frames. These key frames will be transmitted, and from those, the desired sequences selected. As described in Section [BELOW] the choice of a UHF-band transmitter for AOSAT-I forces us to be creative and selective in the transmission of science data.

3.1.2. Science Phase 2

The second and primary phase of the AOSAT-I investigation is to monitor the regolith during a series of centrifuge experiments, and thereby to enable scientists and engineers to validate detailed models for the surface environment of asteroids, comets and small moons. Phase 2 is the novel experimentation of AOSAT, which goes beyond 'microgravity', by which we usually mean 'close enough to zero-gravity that it does not matter', to 'milligravity' by which we mean, 'gravity that is large enough to matter, but only if you have hours to find out'. This is the gravity that determines the geology of small planetary bodies, and AOSAT-I offers the first facility to explore it directly, apart from exploring the surfaces of asteroids themselves in deep space.

3.2. Final Design

The proposed 3U Cubesat (see Figure 2) is designed for operation both in Low Earth Orbit (LEO) and Sun Synchronous Orbit. The spacecraft is built upon a 3U Tyvak frame, functionally partitioned into two sections. A 1U compartment houses the satellite's systems hardware including navigation systems, computers, and communications hardware, while the second, longer chamber is an insertable payload comprising the experimental chamber and required instrumentation, mounted within the spacecraft frame.

The payload chamber has an 8.3 cm^2 cross-section with a length of 19.2 cm and contains an experimental compartment and instrumentation compartment separated by borosilicate glass. The experimental compartment con-
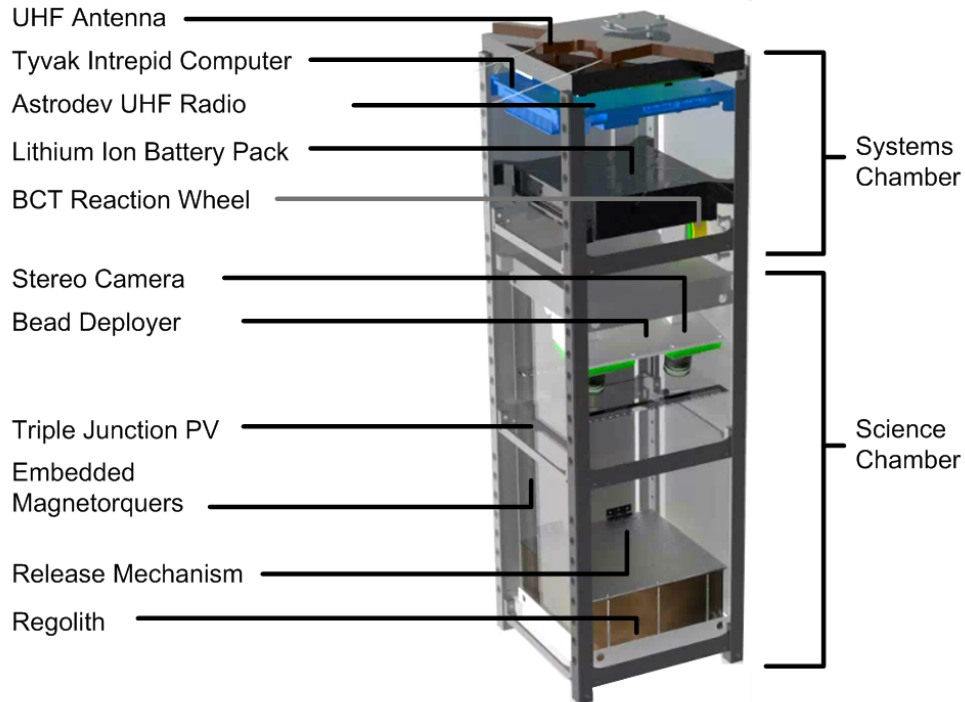
Figure 2: Overview of AOSAT I design specifications.

tains the holding area for the regolith and the spring-loaded burnwire-activated door. The instrumentation compartment of the payload has three cameras, piezo-vibrators and LEDs. This payload does not utilize the full 10 cm^2 cross-section of the satellite but instead is attached inside the frame by mounting brackets due to considerations of structural integrity as well as requirements related to the design of the scientific capabilities.

A high-level overview of system specifications is summarized in Table 1. The mass, volume, and power budget are well within the bounds for CubeSats of this size as required by the Cubesat Design Specification (CDS) [34]. The CDS limits the maximum allowable mass of a 3U craft to 4 kg. The large mass margin ($\sim 25\%$) is attributable to the large hollow experimental chamber required for the regolith experiment. The 9 W power obtained under the sun.

A detailed mass budget for the spacecraft, itemized by subsystem, is pre-

Table 1: Overview of mission bounds

System Specification	
System	3U Cubesat Experiment
Instruments	Stereo Cameras, Reference Camera, Nitrogen Bead Deployer, Piezo Vibrators
Communications	UHF, Simplex Modem
Mass	3050 g
Volume	1300 cm^3
Power	9 W
Payload Mass	1250 g
Payload Volume	450 cm^3
Payload Peak Power	3.7 W
Life	2 Years

sented in Table 2. Note the Chassis kit includes solar array and battery. Note that 0.3 kg of the $\sim$ 1.3 kg payload mass is comprised of asteroid regolith. With such a large margin in the mass budget, the amount of regolith may be adjusted to fit experimental needs. The spacecraft volume (itemized in Table 3) falls within a 61% margin due to the hollow chamber requirement. This provides for design flexibility in order to accommodate additional instrumentation without detriment to experimental results.

The systems chamber contains the Tyvak Intrepid computer, including watchdog circuitry and power control, a Tyvak UHF communications daughterboard, attitude control instrumentation and an S-band communications system. In addition, it contains a reaction-wheel for spinning the spacecraft and three magnetorquers. This allows the CubeSat to generate 1 rpm spin while preventing tumbling and wobbling. The spacecraft will use S-band radio for downlinking science data and will have a maximum data throughput of 115200 bps.

Power will be supplied by the body-mounted photovoltaics and will charge a 37 Whr lithium ion battery. This design allows for all instrumentation and hardware required for spacecraft operations to be integrated within the systems chamber.

One of the limiting factors in designing such systems becomes the total power generated by the solar cells. Power considerations are discussed in

Table 2: Itemized mass budget organized by subsystem

Subsystem	Unit	Mass(g)	Uncert.%	Mass* (g)
Structure	Chassis Kit*	1150.0	30	1495.0
C&DH	Intrepid Board	55.0	30	71.5
Comm.	UHF	21.2	10	23.3
	S-band	64.4	10	70.8
ADCS	Reaction Wheel	110.0	10	121.0
Payload	Cameras	36.0	10	39.6
	Glass	15.4	10	16.9
	Particle Dep.	3.0	50	4.5
	Actuator	22.0	30	28.6
	Mounting Plate	34.0	20	40.8
	Deploy. Mech.	3.2	30	4.2
	Door Assembly	20.0	30	26.0
	Chassis/Mounts	632.2	30	821.9
	Regolith	300.0	0	300.0
			Total Mass	3050
			Standard Mass Limit	4000
			Mass Margin	23%

*Chassis kit includes solar panels and the battery

detail in Section 3.3.5. The requested Sun-Synchronous orbit is projected to generate a total of 192 Whr/day (53.5% within margin), while the less favorable LEO would produce 96 Whr/day (over margin by $\sim 7\%$). It should however be noted that these values are based on maximal concurrent usage of all relevant subsystems. In the case of an ISS orbit, such potential power shortages may be addressed by throttling the power usage.

The 2U science chamber, containing the experimental payload, is detailed in Figure 3. This payload includes three IDS Ul-1646LE cameras, two sets of Yetda white LEDs, a custom micro servo, a particle launcher, and a spring-loaded regolith door activation mechanism utilizing nichrome wire and Vectran. The entire science chamber will be attached to payload mounting brackets (top bracket not shown in the figure) and secured to the Tyvak CubeSat frame.

Within the payload, particle dynamics are imaged by three cameras (one stationary and two servo operated) mounted at the systems end of the science chamber in a protected instrumentation compartment. These cameras can

Table 3: Itemized Volume budget organized by subsystem

Subsystem	Unit	Vol.(cm^3)	Uncert. %	Vol.* (cm^3)
Structure	Chassis Kit*	300.0	30	390.0
C&DH	Intrepid Board	125.5	30	163.2
Comm.	UHF	13.4	10	14.7
	S-band	20.9	10	23.0
Power	37 Whr Battery	194.0	10	213.4
ADCS	Reaction Wheel	33.3	10	36.6
Payload	Cameras	38.9	10	42.8
	Glass	6.9	10	7.6
	Particle Dep.	1.1	50	1.7
	Actuator	8.0	30	10.5
	Mounting Plate	12.6	20	15.1
	Deploy. Mech.	1.2	30	1.6
	Door Assembly	7.3	30	9.5
	Chassis/Mounts	234.2	30	304.4
	Regolith	81.1	10	89.2
		Total Volume		1323.5
		Standard Volume Limit		3400
		Volume Margin		61%

*Chassis kit includes solar panels and the battery

communicate with the computer using serial UART connections. The stationary camera provides a controlled reference view, while the custom servo controls the rotating camera plate with a half-gear integrated on the side of the plate. This allows the stereo pair of cameras an adjustable viewpoint, while maintaining a consistent ocular spacing between them. Separating the instrumentation compartment from the experimental bay is a borosilicate glass window to protect the instrumentation compartment from regolith interference. This also ensures the integrity of the scientific experiments by prohibiting instrumental interference. The glass plate is mounted such that it spans the entire internal cross-sectional plane, allowing for more secure insertion of the plate and providing a convenient mounting location for the LED's as well as a channel for the particle launcher.

The experimental compartment is an 8.3 cm × 8.3 cm × 12 cm laboratory space for the regolith experiments. Regolith is secured in the 2 cm deep regolith reservoir located at the end opposing the instrumentation section. The

Figure 3: Illustration of scientific payload design oriented with sealed regolith chamber on the bottom and all instrumentation protected behind borosilicate at top.

0.3 kg of asteroid material is held back by the regolith door via a Vectran fiber loop. In a small "attic" chamber adjacent to the regolith, a spring loaded nichrome wire resister is placed through this loop. When activated, springs will pull the heated resistor taut against the wire and cut through it. The torsional springs on the door hinge will then bring the door to its open position, recessing it into the cubesat wall in order to minimize obstacles which may interact with the regolith particles. The regolith reservoir measures 2 cm × 8.3 cm × 8.3 cm. After door deployment, 20 mm diameter, tunable (up to 6.3 kHz) patch vibrators (not shown) mounted in a distributed array on the outer edge of the regolith chamber (underneath the regolith in Figure 3) will impart the regolith with kinetic energy, slowly translating it into the experimental chamber prior to execution of microgravity experiments.

3.3. Subsystems

We now describe the Subsystems of AOSAT-I beginning with a description of the science payload and deployment, the cameras that acquire the primary data, and the ADC system that must meet the requirements of diverse experimental configurations from $\sim 0-1$ rpm. The rotating spacecraft must also be able to generate sufficient power and be able to transmit its data back to Earth, and to be of low risk in overall redundancy and design.

3.3.1. Payload

Both of these stages will be monitored with a stationary camera and tilting stereo camera pair driven by a servo. Image frames are the primary data product of AOSAT-I. The incorporation of a tilting camera system with a stationary camera ensures that occlusion of experimental details will be reduced, and allows for various stereo angles centered on specific geometries within the chamber.

3.3.2. Door Mechanism

The door mechanism relies on a single door and a slightly smaller regolith holding area. This well-tested mechanism [REFS?] will be miniaturized to fit within a small hidden chamber above the regolith area, recessed in this wall extension as shown in Figure 4. This restraint system is secured near the door edge, furthest away from the hinge. During the first stage of the mission, the nichrome wire will heat and cut the Vectran restraint, releasing the the door and allowing the torsion spring hinge to open the chamber. The door will swing down into the floor of the chamber and become flush.

3.3.3. Optical Instruments

Imaging of particle dynamics within AOSAT I is done by a static camera placed in one of the bottom corners of the instrumentation chamber (see Figure 5) and two additional cameras attached to a hinged plate with a torsional spring with a servo affixed beneath. Because there was not enough space for a gear attached directly to the hinge, part of the plate was an embedded half-gear. This pseudo-gear is centered on the hinge axis so that it can rotate as a typical gear would, providing camera tilt for the stereo vision pair of cameras. This single servo reduces power draw as well.

A preliminary trade study investigated various camera system options for AOSAT I, with preference given to camera systems with space heritage. A high-resolution camera system was required in order to meet all science
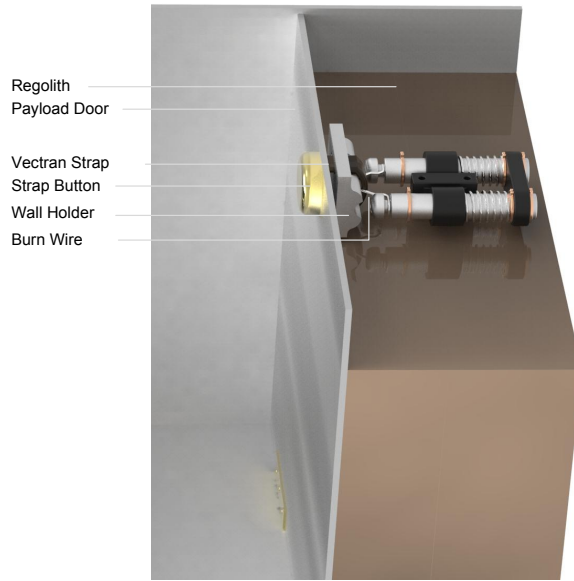
Figure 4: Illustration of regolith retention door apparatus utilizing nichrome burn-wire mechanism. Wall between regolith and mechanism has been turned transparent.

mission objectives, including capturing image data of coarse particle aggregation over time. Results of the trade study are summarized in Table 4. The specific camera selection is driven by the requirement to image the entire lab chamber, but especially the back side of the chamber. One of the advantages of AOSAT design, is that the lab chamber can be developed quite independently with the use of low cost engineering models, and the final camera choice will be decided by reproducing the exact same experiments that will be flown. At the same time, we are developing the analysis tools for key image frame detection (onboard the spacecraft) and image post-processing analysis.

Owing to payload limitations on size and mass, the IDS UI-1646LE by IDS Imaging Development Systems (first column in Table 4) was selected. Through ground experiments with a model of the AOSAT I spacecraft and purchased preliminary cameras, optimum pixel dimensions of the still images are being be assessed. Camera mass, footprint, and fps features were taken into account to ensure optimum performance of the camera instrumentation. Thermal analysis (the subject of a future paper) has been done for the spacecraft and shows the camera will be well within in its operating temperature at all times.

Table 4: Detailed camera trade study

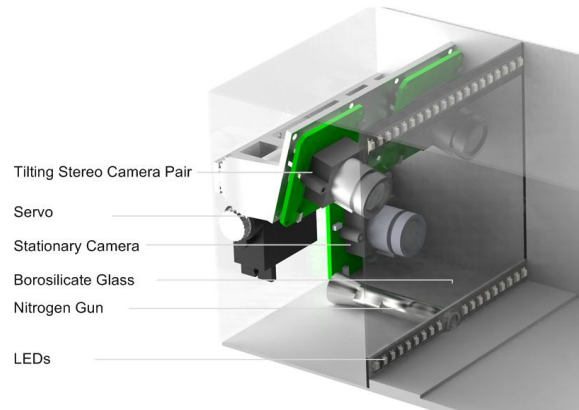| Camera	IDS UI-1646LE	NanoCam C1U 3 MB	Kodak MCM20027	HTC Evo & LG Optimus	μCAM TTL Omnivision
Pixels (MP)	1.3	3	1.3	1.3	0.3
Pixel Dim.	1280 × 1024	2048 × 1536	1280 × 1024	1280 × 1024	640 × 480
Capture Rate (fps)	25	20	10	30	30
Technology	CMOS	CMOS	CMOS	CMOS	CMOS
Interface	USB 2.0	I^{2}C	I^{2}C	N/A	TTL
Mass (g)	12	166	20	< 10	6
Flight Heritage	MCUBED, Michigan U.	multiple	AAUSAT, Alborg U.	N/A	multiple
Footprint (cm)	3.6×3.6×1.0	9.6×9.0×5.8	2.4×2.4×1.0	3.6×3.6×1.0	3.2×3.2×2.1

Figure 5: Illustration of final three camera design incorporating a single fixed camera and two cameras affixed to a rotating plate.

3.3.4. Attitude Determination and Control

Maintaining attitude control of AOSAT I is a critical requirement during the centrifuge experiments. For instance, the shifting regolith within the experimental chamber of the spacecraft results in a dynamic center of mass, potentially causing nutations of the satellite. During the centrifuge experiments, the spacecraft will be spinning at 1 rpm with respect to its primary axis. Following the conventions of orienting body and orbit frames, this rotation axis will be the body x-axis for AOSAT I, and the rotation angle (Euler angle) will be referred to as roll.

AOSAT I will employ an onboard inertial measurement unit (IMU) which consists of a 3-axis accelerometer in addition to the onboard BMA250. Unfortunately the BMA250 cannot sense the required 1 rpm and hence we are using a second accelerometer that can operate in ranges varying from ± 1 **g** to ± 16 **g**; a gyro (L3G4200D) with operating range from $250°/s$ to $2000°/s$, and a 3-axis magnetometer (HMC5883L) which operates within a full scale range of ± 8 G. These sensors can be tuned for various operating ranges, sensitivities and sampling periods. A similar IMU (GY-80 from Shenzhen Guangshun Electronics), which has the same gyro and magnetometer but a different accelerometer (ADXL345), is presently being used for in-laboratory testing, as a substitute for the on-board IMU. All the sensors are being collectively sampled at a rate of 100 Hz with the following settings:

- accelerometer range of ± 16 **g** and a sensitivity of 0.03125 m**g**/LSB

- gyro range of 500°/s and a sensitivity of 17.5 mdeg/s/LSB

- magnetometer range of ± 1.3 G and a sensitivity of 0.92 mG/LSB

The attitude control actuators of AOSAT I consist of three mutually perpendicular built-in magnetorquers and one reaction wheel oriented along the desired spin axis. Each magnetorquer is capable of generating a magnetic dipole moment of magnitude 0.1 Am^2. The reaction wheel is a Blue Canyon RWp 015 micro reaction wheel. This serves the dual purpose of compensating in the event of under-actuation by the magnetorquers, which may occur when the spacecraft traverses regions in which the earth's magnetic field becomes parallel to any of the magnetotorquers, and also during operation in the centrifuge mode. This reaction wheel weighs 0.11 kg and can produce a maximum torque of 0.006 Nm.

With the actuators and the sensors discussed above, the dynamic model of AOSAT I can be modeled with the net external torque (τ_{net}) defined as

$$\tau_{net} = \tau_c + \tau_d \ = I_s * \dot{\omega}_s \ + \ I_{rw} * \dot{\omega}_{rw} \ + \ [\omega_s \times] * I_s * \omega_s \ + \ [\omega_s \times] * I_{rw} * \omega_{rw} \quad (1)$$

where τ_c is the control torque from the magnetorquers, τ_d is the disturbance torque from various sources, I_s is the Inertia matrix of the satellite, ω_s is the angular velocity vector of the satellite with respect to Earth, I_{rw} is the Inertia matrix of the reaction wheel, and ω_{rw} is the angular velocity vector of reaction wheel with respect to Earth. The notation $\dot{\omega}$ denotes the time derivative of the parameter ω, and the notation $[\omega \times]$ denotes an operation called skew symmetric version of the vector $[\omega]$. The product of the skew symmetric version of any vector ($\vec{A}$) with another vector ($\vec{B}$) is equal to their cross product, i.e.,

$$[\vec{A} \times] * \vec{B} \ = \ \vec{A} \times \vec{B}$$

AOSAT I uses only one reaction wheel, the angular velocity of the reaction wheel is be given by the vector

$$\omega_{rw} \ = \ \begin{bmatrix} \omega_{rwx} \\ 0 \\ 0 \end{bmatrix},$$

where ω_{rwx} is the angular velocity of the wheel about the satellite X-axis. The single reaction wheel also simplifies I_{rw}.
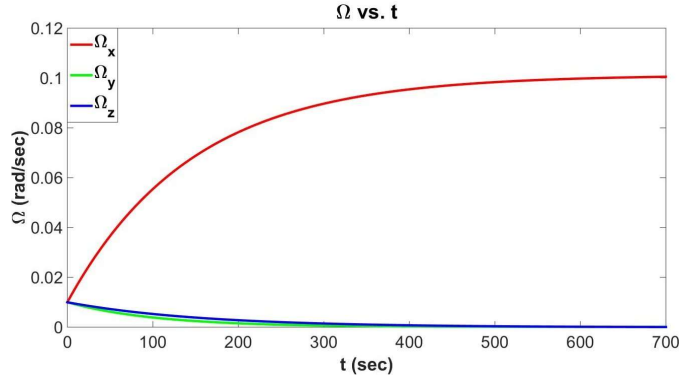
Rearranging Equation 1, yields the nonlinear dynamic model for AOSAT I:

$$\dot{\omega}_s \;=\; -I_s^{-1} * \left(I_{rw} * \dot{\omega}_{rw} + [\omega_s \times] * I_s * \omega_s + [\omega_s \times] * I_{rw} * \omega_{rw} \right) + \tau_d + \tau_c. \quad (2)$$

Equation 2 illustrates the relationship between the desired state (ω_s), and the control terms $(\omega_{rw},$ and $\tau_c)$ under external forcing, in the form $\dot{x} = f(x, U)$. A linear control law of the form $U = Kx$ was used for simulating the model, and to test control response.
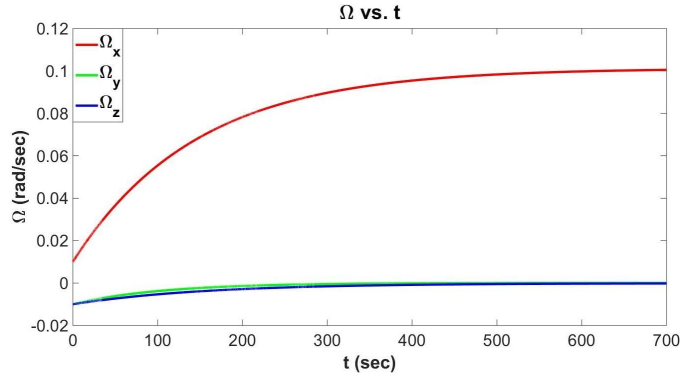
(a) Test-1

(b) Test-2

Figure 6: Attitude control on Roll axis for test conditions summarized in Table 5.

Figure 6 shows the attitude response of two simulations that were run with different conditions (summarized in Table 5). The results suggest that, with the proposed controller, the model is robust to disturbance torques of magnitude 3.4×10^{-7} Nm caused by gravity and solar radiation pressure.

21

Table 5: Simulation Results

Parameter	Test 1	Test2
Initial conditions (rad/sec)	$\omega_x = 0.01$ $\omega_y = 0.01$ $\omega_z = 0.01$	$\omega_x = 0.01$ $\omega_y = -0.01$ $\omega_z = -0.01$
Final conditions (rad/sec)	$\omega_x = 0.1$ $\omega_y = 0$ $\omega_z = 0$	$\omega_x = 0.1$ $\omega_y = 0$ $\omega_z = 0$
Disturbance torque (Nm)	3.4×10^{-7}	3.4×10^{-7}
Settling time (sec)	575	575
Reaction wheel acceleration (rad/s^2)	25	25
Magneto-torquer Current (A)	3	3
Energy Consumption (Whr)	2	2

Figures 6a and 6b show that the roll rate of the satellite settles to 0.1 rad/s ($\approx$ 1 rpm), in less than 600 s with a pointing accuracy of 2°. This controller required 2 Whr of power with an error of 0.3 rpm. It is possible to further reduce the settling time by providing additional power. For instance, an additional 1.5 Whr resulted in a settling time of 300 s.

3.3.5. Power

The AOSAT I power system architecture relies on the electrical power system capabilities integrated with the Tyvak flight computer and supplemented by a 3.7 V lithium-ion battery pack, storing 37 Whr of energy. Modeling of system energy consumption indicates that AOSAT I lies within power budget margin for both sun-synchronous and ISS deployment orbits. The power budget is summarized in Table 6. Calculations based on peak optimal duty cycles for spacecraft subsystems and payload instrumentation yield an energy consumption rate of $\sim$ 80 Whr/day. The International Space Station deployment orbit produces nearly 100 Whr/day, which gives a 17% power margin, while sun-synchronous orbit yields 190 Whr/day and so there is excess power. Duty cycles for this calculation assume peak onboard data processing, scientific operation and radio communication throughout the course of a standard operational day. Basic spacecraft functionality consumes 33 Whr/day, leaving sufficient energy for scientific operations with either orbit.

Table 6: Itemized AOSAT I Daily Power Budget

Subsystem	Duty Cycle	Unit	Power (W)	Energy (Whr)
C&DH	1.0	Intrepid System	0.1	2.9
Comm.	0.1	UHF	1.5	3.6
	0.1	S-Band	10	24
ADCS	0.5	Reaction Wheel	2	24
	1.0	Magnetorquer	0.1	2.4
Science	0.2	Cameras	0.8	3.6
	0.04	Piezo	0.1	0.1
	0.2	LED Array	2.9	14
Data	0.6	Intrepid System	0.5	7.2
Total Energy Consumed Per Day				80
Energy Generated Per Day (ISS)				96
Energy Margin Per Day (ISS)				17%
Energy Generated Per Day (Sun-Sync)				190

3.4. Communications

Determination of an effective communications system required detailed analysis of the prospective spacecraft orbits and ground station coverage. Using AGI's System's Tool Kit (STK) software, the requested Sun-synchronous orbit of 450 km × 810 km at 97.2° inclination was propagated in order to generate coverage estimates. Coverage modeling required propagation of AOSAT I's estimated location and altitude during the first 30 days after deployment on the proposed trajectory. Appendix A includes details on the link budget calculations and this includes link budget for UHF, Figure A.13 and S-band, Figure A.14. The calculations are respect to the elevation angles (0° to 90°). The primary location for AOSAT I ground station communication will be Arizona State University (ASU), although other locations have been considered.

The coverage analysis for ASU's location yielded a minimum access time of 113 s (2.88 min.), a maximum access time of 928 s (15.5 min.) and a mean access time of 633 s (11 min.). The orbit results in approximately 5 passes every 24 hrs, averaging approximately 52 min. per day to downlink data. Utilizing ASU as the only ground station would restrict daily communication to 3.0-3.8% of the orbit, corresponding to approximately 13-16 MB per day using a 38400 bps data rate and about 38-48 MB per day using a 115200 bps

data rate.

Incorporating partner ground stations would increase coverage and provide higher data throughput. Table 7 shows an average time (in seconds) the AOSAT I will be above 0° elevation angle with respect to various points on earth.

Table 7: Approximate access times(in seconds) for 4 earth locations over 30 days

Obit Type	ASU	Seattle	Fairbanks	New Zealand
Sun-Sync	100,000	140,000	250,000	85,000
ISS	100,000	100,000	45,00	120,000

AOSAT I will have two communications systems including a UHF and S-band. The primary communication system is the UHF transmitter/receiver provided by Tyvak. This board is easily integrated with the Tyvak hardware and software suite, making it a reliable primary communication system. The UHF platform communicates via a deployable L-dipole antenna, integrated into the Tyvak hardware suite. UHF data transmission will consist of downlinking spacecraft operating parameters and uplinking commands for payload experiments. The secondary communication system will handle downlinking experimental data and telemetry.The s-band transmitter is Quasonix nanoTX, which supports frequencies between 1.4-2.2 GHz and is in a small form factor(20.89 cm^3), and has a proven track record alongside the Tyvak Intrepid System Board.

3.4.1. Command and Data Handling

The Tyvak Intrepid System Board (shown in Figure 7) acts as the command and data handling controller onboard AOSAT I. The Intrepid platform, produced by Tyvak Nano-Satellite system Inc., provides an integrated command and data handling architecture, as well as an electrical power system, in a CubeSat form factor. This model is CDS compliant with and meets all required specifications relevant to the Poly Picosatellite Orbital Deployer (P-POD). Intrepid is specifically designed with terrestrial development in mind with the end objective of small, lightweight spacecraft. The system board comes with an umbilical development board that handles debugging, terminal I/O, power and efficient board access even while integrated into the final mission form factor. Tyvak Intrepid has a flight legacy with 3 CubeSats

currently in orbit from the TLS-01 mission and is a system board for NASAs INSPIRE interplanetary CubeSat.

Figure 7:   Tyvak Intrepid System Board.

Intrepid, comprised of a main system board and additional breakout utility specific boards, will act as a centralized computational center for all data, communications and spacecraft specific command handling. Data is handled via SPI, USB, UART and I2C busses and stored in an SQLite database and integrated high capacity MicroSD card. Intrepid provides multiple bus solutions under each interface to streamline the separation of spacecraft avionics commands from payload specific operations.

3.4.2. Data Processing

Owing to the limitations of AOSAT I communications bandwidth and our need to quantify particle motion, it is critical to develop an algorithm to identify, track, record, and transmit the evolution of suspended particles to the communications ground station. Our technique utilizes algorithms that exploit particle reflectivity and shadowing in order to identify and track the particles of interest. This will enable us to place LED lights at an optimal location within the CubeSat, thus allowing the camera system to aid in the particle detection process. Our studies show a minimum of a 50-fold savings in data bandwidth for tracking and detection of dust particles compared to conventional, non-lossy compression image capture.

Our particle tracking technique utilizes algorithms written in Matlab and tested in ground experiments that will exploit particle evolution and motion

over time in order to identify and track the particles of interest. The utilization of both Lucas-Kanade [35] and Horn-Schunck [36] optical flow estimation methods are key in accounting for displacements of particle groupings on a range of scales. For every pixel in the region of interest, a motion vector is calculated in both the x and y directions. This allows mapping of one pixel through a series of frames. The particle optical flow code assigns a movement vector (u,v) to every interesting pixel, yielding a flow field, both true color and colorized. Sequences of images captured over time will be processed and analyzed for noise, motion, shadowing, and particle statistics, aiding in constraining the parameters of the code and data analysis.

Use of multiple cameras allows for depth of field to be calculated and processed. This data is significant for early verification of expected aggregate distribution with respect to the spacecraft center of mass, as well as to meet scientific objectives pertaining to particle accretion. In similar equidistant intervals to the particle tracking frames, the Tyvak Intrepid will take stereo image pairs to determine current particle distribution inside the experimental chamber. This process is illustrated in Figure 8.

Command-driven software protocols allow for the downlink of individual frames, index ranges, or complete experimental data sets. These commands, transmitted to the spacecraft via UHF, initiate the transfer of images specified from the database to the downlink queue, stored on the MicroSD memory card. Once the command has been received, the Tyvak Intrepid processes the command data and transfers the requested section of scientific data from the storage database to the downlink queue. Scientific data is prioritized last, behind spacecraft telemetry data and initial experimental keyframe science downlinks, as these are needed to maintain ongoing spacecraft operations and plan future experiments, respectively.

The mission profile includes three phases of science operation (Table 8). The first phase of operation begins with door actuation, releasing the meteorite aggregate into the science chamber. The door deployment will be photographed in stereo for 30 seconds at 25 frames per second (the operating limitation of the camera), followed by stereo images being recorded for 10 minutes at 1 frame per second. The second mission phase includes three microgravity experiments to monitor meteorite particle aggregation over different periods of time ranging from four to fifteen hours, with data being collected in stereo at a maximum frame rate of 6 frames per minute. The final mission phase will consist of eleven experiments, utilizing the centrifuge capability of the spacecraft to produce varying gravity fields to monitor pack-
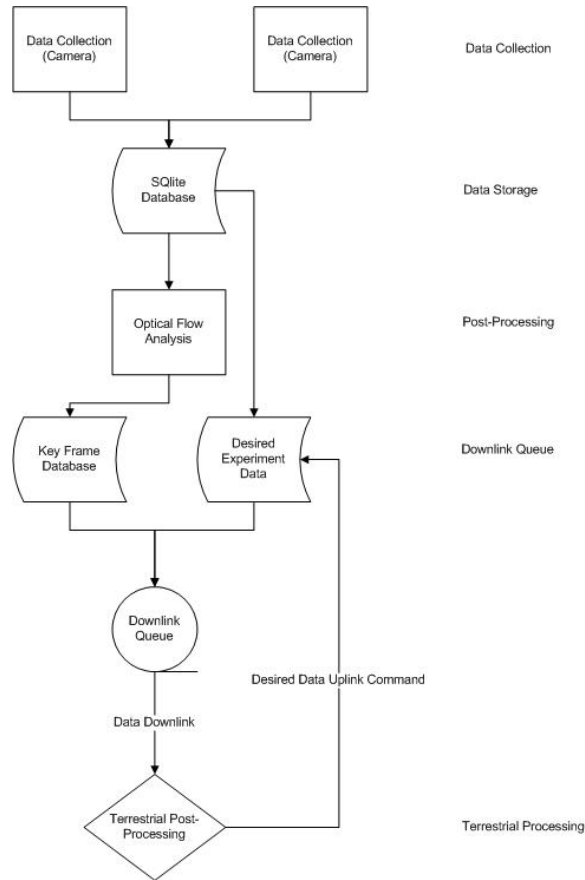
Figure 8: Graphical depiction of data handling procedures.

ing of asteroid Regolith. Impact dynamics will be monitoring during starting and stopping of the centrifuge capability. Experiments will last one hour and data will be recorded in stereo at 15 frames per minute. In each of these phases, a certain number of key frames will be recorded. Key frames are meant to convey the state of the experiment at a glance. For the door deployment phase, there will be 340 key frames. The total number of frames generated will be 1350 frames over the duration of door opening sequence. Key frames are interspersed during each experiment or phase and are not taken at regular time intervals. A key frame is made by monitoring the Shannon's entropy of particle spatial distribution in the experimental area [37, 38]. This algorithm will be used to determine the Shannon's entropy of the particles in the experiment chamber volume. When particles aggre-

gate, the Shannon's entropy decreases and it increases if the particles are dispersed. A major change in Shannon's entropy is of interest to us and is used to trigger recording a key frame. Afterwards, the changes in Shannon's entropy is ranked and the top 340 is downloaded for the door opening sequence. A lot more key frames are generated for the door open sequence to help validate the key frame generating algorithm before the science experiments start. Out of the 1010 frames generated, twenty two percent of the non-key frames will be downloaded and is 225 frames. For the microgravity experiments, 100 key frames will be generated over the 3 experiments. Furthermore 3,333 non-key frames will be generated for each experiment and equally timed over the length of the experiment.

For the impact dynamics and centrifuge experiments, 275 key frames will be generated over the 11 individual experiments. Therefore the total number of frames downloaded is the sum of the key frames and total frames produced multiplied by the fraction to be downloaded. The total number of frames downloaded from all three missions phases is 4,390 frames and each stereo pair of images is presumed to be 300 Kb. The total amount of data to be downloaded is 1.5 GB and includes 0.18 GB science data margin.

4. Feasibility Experiments

The behavior of regolith and rocks in low gravity is important to the understanding of primary accretion, asteroid surface properties, and for hazardous asteroid mitigation work. In order to better understand how regolith and rocks behave in low gravity, we have developed the Astrophysical Rubble piles Simulation Software (ARSS), utilized ground experiments testing neutrally buoyant beads and water in an experimental cubesat, and imaged particle-shake tests in order to test the particle tracking method with varying grain sizes.

4.1. Particle Simulations

Particle simulations support mission operations in developing models of anticipated interactions of regolith particles and in planning for guidance navigation and control scenarios. Understanding the physical interactions of particles under different gravity conditions allows for better understanding of settling time during different experimental phases of the mission. This information allows for better mission planning for both scientific results and engineering spacecraft stability. Bead deployment from the nitrogen blower

Table 8: Theoretical data volume for primary mission

Experim. Phase	# of Exp.	# Key Frames	Non Key Frames Prod.	Fraction d/l	Frames d/l
Door Deploy.	1	340	1010	0.22	565
Microgravity Experim.	3	100	10000	0.25	2600
Impact Dynamics & Centrifuge	11	275	9625	0.13	1225

Data Per Frame	300 Kb
Total Mission Frames	4,390
Margin	0.18 Gb
Total Mission Data	1.5 Gb

and the initiation of the centrifuge both contain relatively large uncertainties as these experiments cannot be accurately modeled under the conditions of terrestrial gravity. To reduce uncertainty related to particle interactions during these events, relevant parameters were modeled to best calibrate the scientific instruments and spacecraft stability system.

Particle interactions were modeled with the PhysX physics engine as part of the Nividia CUDA development environment. Utilizing graphical processing units (GPUs), models of a collisional environment can be generated in order to investigate the effect of differing values of parameters such as gravity, particle density, elasticity, and particle density.

Such simulations were conducted, defining parameters to model the operating environment of the payload chamber in low gravity conditions with particles similar to the meteorite regolith contained in the AOSAT I science payload. These simulations were comprised of $33,000$ individual particles with a diameter of 0.313 mm inside a 2 cm^3 domain. The simulation domain consists of 643 grid spaces in each direction, with each cell consistent with the diameter of a particle. Uniform grid subdivision is utilized to determine particle to particle interactions. This bound limits the number of particles in three-dimensional space which can inhabit any one grid cell to 4. Additionally, the number of cells a single particle inhabits at any given instant is also constrained to 8. The center location of the particle determines its primary cell which is then utilized to determine relevant particle interactions with all inhabiting particles.

Initiation of centrifugation generates significant uncertainty in the center of mass of the laboratory-spacecraft, and consequently there are issues we have had to address concerning the guidance and control of AOSAT I. Modeling the particle interactions with varying centripetal accelerations allows for further insight into particle settling time, and thus, further terrestrial refinement of the AOSAT I attitude control algorithms. A series of particle simulations were undertaken with varying magnitudes of artificial gravitational acceleration in order to investigate the dynamics of the regolith sloshing within the science chamber due to the spacecraft rotation. Results are shown in the sequential images of Figure 9, illustrating the distribution of particles at various times (as noted in each panel) corresponding to gravitational accelerations of 0.01 **g** (Fig. 9a), 0.001 **g** (Fig. 9b), and 0.0001 **g** (Fig. 9c).

The longest particle settling time observed was 75 s under an acceleration of 0.0001 **g**. In all scenarios, the majority of the regolith transferred to the

aft of the science chamber within 20 s of centrifugation. This mass distribution is comparable to the launch configuration with the particles packed in the area below the door. The rate of spin-up for the centrifuge must be calibrated against data inferred from the particle simulation data to reduce significant perturbations produced by particles packing with too large of an initial velocity. Conversely, a spin-up that is too slow will result in a lengthy settling time. While a lengthy settling time does not interfere with science objectives, it is important to know the settling time so that we can know when and for how long to turn on the cameras for data acquisition.

(a) 0.01 **g**
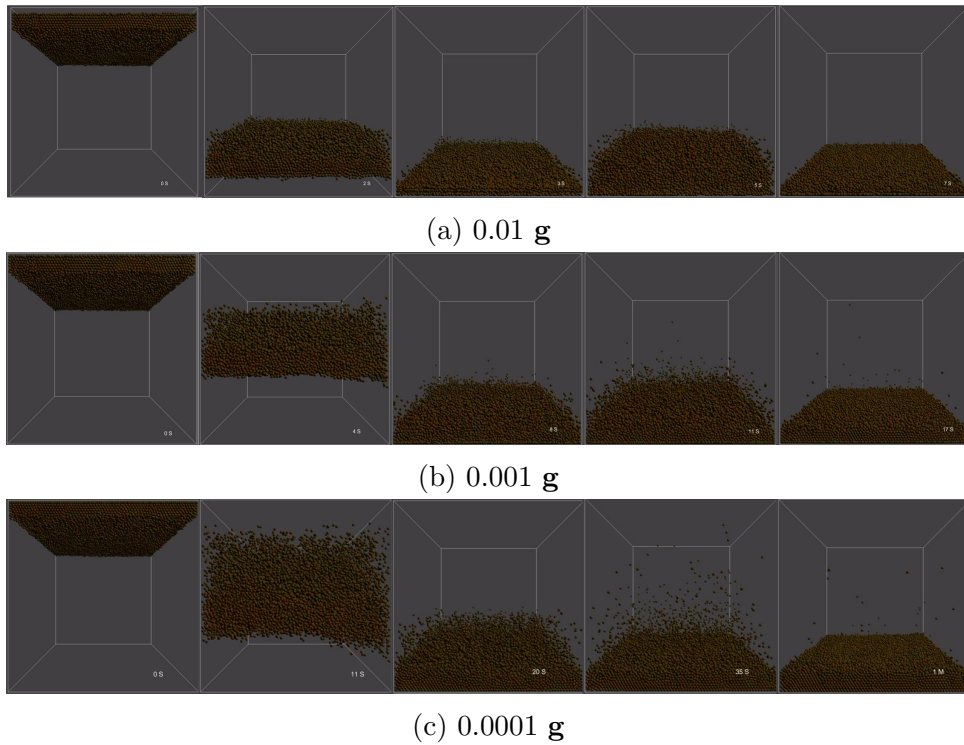
(b) 0.001 **g**

(c) 0.0001 **g**

Figure 9: Time sequence of particle settling dynamics under gravitational accelerations of 0.01 **g** (top panel), 0.001**g** (middle panel), and 0.0001**g** (bottom panel).

4.2. Particle Dynamics Using CubeSat Centrifuge Model

For the proposed AOSAT I experiment, we developed an analogue to better understand particle behavior in a rotating centrifuge. This analogue is not meant to test the physics but to help conceptualize the experiment and

visualize data acquisition. For this purpose, a neutral buoyancy model was built and tested. The model utilized a fully sealed plexiglas chamber containing water and near-neutrally buoyant microspheres made from polyethylene which had a density slightly higher than water (Figure 10). The model contains a camera attached to provide an overhead view of the experiment chamber. The model CubeSat is spun horizontally about its short axis such that the resulting centrifugal force pushed the microspheres outwards.

The water and beads settled into an equilibrium steady-state after approximately 45 seconds. As the spacecraft model rotated with angular velocity of 15 rpm, the beads were observed to have accelerated toward the far end of the chamber by overcoming fluid drag, accelerating opposing the axis of rotation at $a_{bead} \sim 3 \times 10^{-3}$ cm s$^-$2. This slow movement (compared to the expectation in a spacecraft spinning that fast) is due to the low inertia beads, fluid drag and turbulence of the fluid; again this is not a physical comparison. The bead particles cluster at the edge of the chamber, away from the axis of rotation, and collect around the chamber far edges as shown in Figure 11. This observation shows similar trends to the particle simulation work shown earlier [39].
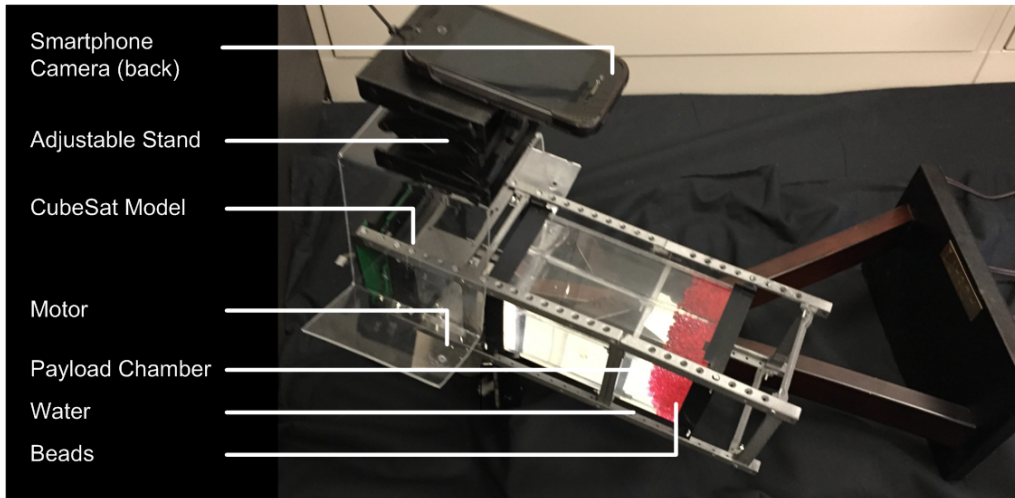

Figure 10: Layout of the CubeSat centrifuge model.

Overall, the objectives of this experiment were two-fold. The first objective is to better predict asteroid regolith action in space for experimental design and data acquisition. The second objective is to compare how a simulated test in a neutral buoyancy laboratory can, in general, provide insight

32

into milligravity centrifuge experiments. For instance, on the basis of these studies we expect that the regolith particles inside AOSAT-I will not all settle at the far wall of the chamber. Instead we might anticipate that most will cluster initially at the far edge, and a certain portion will accumulate at the corners, prior to using the vibrator to flatten and disperse the regolith bed.
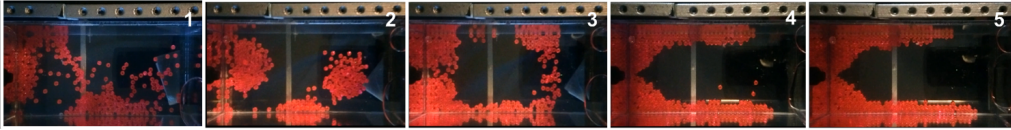

Figure 11: The right side of the chamber is closest to the spin axis. As the chamber is spun at a rate of 15 rpm, the particles start to migrate and deposit towards the outer edges. This evolution of particle position is shown at time =0, 3 seconds, 7 seconds, 17 seconds, 21 seconds and 27 seconds.

5. Discussion

In this work we demonstrate the preliminary feasibility of a CubeSat centrifuge to perform simulation of asteroid surfaces. The spacecraft, when not spinning, will be used to conduct regolith aggregation experiments. Through our design process, we have identified off the shelf components including the Tyvak CubeSat bus, S-band communication system, Blue Canyon Reaction Wheel and solar panels embedded with magneto-torquers. Using these components, we can simplify the design and development of the proposed laboratory. A science payload will be developed in-house and be instrumented with 3 cameras, contain a packaging system for carrying the regolith into space and will have a bead deployment instrument, that will release bead into a simulated asteroid surface formed from the regolith settling at the edge of the chamber when the spacecraft is spinning.

We considered multiple designs including an asymmetrical two chamber design, a two chamber symmetrical design and a single chamber design. A single chamber design offers low development risk and is overall simpler to implement with sufficient volume margins for the science instruments. The key determining factor is that the payload chamber be large enough to permit observation of the regolith while reducing concerns of occlusion and wall/edge effects. A single chamber design however requires more power be expended in lighting the chamber.

33

In our proposed system, we will use the magnetorquers to hold the CubeSat pinned to the Earth's magnetic field lines and then use the reaction wheel to spin it about the minor axis. Through this work, we demonstrate that it is feasible and that we have enough control authority to prevent unwanted tumbles, and sufficiently rapid settling time.

Overall, the system is feasible, with a mass margin of 23%, volume margin of 60% and 45% energy margins when deployed on a sun-synchronous orbit. On an ISS orbit, there is a negative energy margin and this would require delaying certain science experiments and thus stretching out the primary mission. Overall, both ISS and sun-synchronous orbits are viable for the proposed concept. Software simulation of regolith particles show the feasibility of simulating low-gravity particle interactions. Further work was done using a model of a CubeSat to demonstrate the centrifuge effect. Plastic beads in water simulated the low gravity conditions. The results support observations that most of the regolith will settle at the furthest wall edges, but some of the regolith will cling and settle at the payload chamber walls.

For the proposed mission, utilizing only the UHF antenna and our main ground station for communication poses significant challenges in communicating the primary science data over a 1 month period. Our studies show that data reduction methods can be used to transmit the highest priority science data using UHF alone. However this is insufficient for transmitting video. The situation improves if we network our ground station with others to increase daily coverage. The situation further improves if an S-band communication were to be used. Overall, our studies shows a promising development pathway for the assembly and testing of the AOSAT I CubeSat mission for demonstration of the two major mission objectives, namely to demonstrate regolith aggregation in space and for demonstrating a centrifuge laboratory in microgravity.

6. Conclusions

In this paper we propose development of AOSAT I, an on-orbit, 3U (34 × 10 × 10 cm), 4 kg CubeSat centrifuge, designed to simulate asteroid surface conditions. Demonstration of this CubeSat will provide a low-cost pathway to physical asteroid model validation, shed light on the origin of asteroids, and constrain the design of future landers, rovers, and resource extractors. AOSAT I will house crushed meteorites (remnants of asteroids) and enable scientific experiments within its payload chamber while operating in two dis-

tinct modes: 1) a centrifuge producing artificial gravity to simulate surface conditions on asteroids of diameter up to 20 km, and 2) as a stationary microgravity laboratory to investigate primary accretion. Analysis of the feasibility of this proposed spacecraft shows healthy mass, volume and energy margins for a sun synchronous orbit. The system will be built mostly of off-the-shelf components, except for the payload chamber, consisting of custom camera, a regolith container and bead deployer that will interact with regolith. Simulation of the proposed attitude control system shows that spacecraft can spin between 0 to 4 rpm to produce the required centrifugal force, without risk of tumbling. The proposed system illustrates the effective use of low-cost, off-the-shelf components in the rapid assembly and instrumentation of a CubeSat science laboratory. Successful demonstration of this science laboratory can open the pathway to more ambitious missions to simulate a wider range of 'gravity', from the smallest asteroid to the Moon and larger bodies, for applications in life-sciences, materials testing, manufacturing, planetary geology, and 3D printing in space.

Appendix A. Link Budget

This following section shows calculation of the link budget for the AOSAT 1 spacecraft. Figure A.12 shows the position of the spacecraft relative to the ground station and Figure A.13 shows detailed Uplink and Downlink budget for UHF communication. Figure A.14 shows detailed Uplink and Downlink budget for S-band communication.

Boltzmann Constant: $k_B = -228.6 \frac{\text{dBW}}{\text{Hz} * \text{K}}$
Speed of Light: $C = 299792458 \frac{\text{m}}{\text{sec}}$
Mean Radius of Earth: $k_E = 6378140$ meters
Mean Orbit Radius of AOSat: $k_A = k_E + \frac{\text{Perigee} + \text{Apogee}}{2} = 6378770$ meters
Mean Orbit Radius of Globalstar: $k_G = k_E + 1414 = 6379554$ meters
Elevation angle: δ_1 or $\delta_2 = $ (variable) degrees
Frequency: $f = $ (variable) Hz
Data Rate: $R_D = $ (variable) bps
Transmit Power: $P_{TX} = $(variable) Watts
Data Bandwidth relative to one Hertz: $\text{RdBW} = 10 * \log_{10}(R_D)\text{dBHz}$
Frequency Wavelength: $\lambda = \frac{C}{f}$ meters
Slant Range for ground station:
$S_1 = k_E * [\sqrt{k_A^2/k_E^2 - \cos^2(\Pi * \delta_1/180)} - \sin(\Pi * \delta_1/180)]$
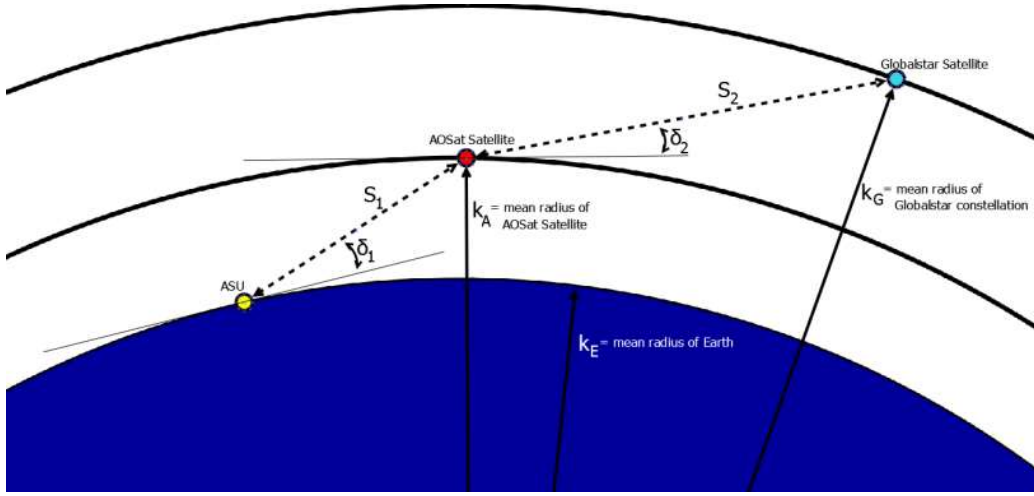*Slant Range for Globalstar satellite:*

Figure A.12: Diagram for link budget

$S_2 = k_A * [\sqrt{k_G^2/k_A^2 - \cos^2(\Pi * \delta_2/180)} - \sin(\Pi * \delta_2/180)]$

Transmission Line Loss: $T_x LL$ = (variable) dB

Power at Antenna: $P_A = (10 * \log_{10} P_{TX} - T_x LL)$ dBW

Transmit Antenna Gain: TxGain = (variable) dBi

Effective Isotropically Radiated Power: EIRP $= (P_A + \text{TxGain})$ dBW

Path Loss: $L_{\text{path}} = \left(22 + 20 \log_{10}\left(\frac{S_i}{\lambda}\right)\right)$ dB

Atmospheric Loss: $L_{\text{atmosphere}}$ = (variable) dB

Antenna Pointing Loss: L_{pointing} = (variable) dB

Polarization Loss: $L_{\text{polarization}}$ = (variable) dB

Ionospheric Loss: $L_{\text{ionospheric}}$ =(variable) dB

Total Path Losses:

$L_{\text{total}} = (L_{\text{path}} + L_{\text{atmosphere}} + L_{\text{pointing}} + L_{\text{polarization}} + L_{\text{ionospheric}})$ dB

Incoming Isotropic Sound Level: ISL = EIRP $- L_{\text{Total}}$ dBW

Receive Antenna Gain: $(R_x \text{Gain})$ = (variable) dBi

Receive Line Loss: $(R_X LL)$ = (variable) dB

Noise Temperature: (k_T) = (variable) K

Figure of Merit: $(\frac{G}{T}) = [R_X \text{Gain} - R_X LL - 10 \log_{10}(k_T)]\frac{\text{dB}}{\text{K}}$

Signal to Noise Power Density: $(\frac{S}{No}) = (\text{ISL} + \frac{G}{T} - L_{\text{pointing}} - k_B)$ dBHz

Energy per bit to Noise Power Density: $(\frac{Eb}{No}) = [\frac{S}{No} - 10 \log_{10}(R_D)]$ dB

Required signal strength for Modulation: (M_T) = (variable) dB

System Link Margin: $= \left[\frac{Eb}{No} - M_T\right]$ dB

UHF Downlink Budget (EbNo Method)					
Software/ Configuration Parameters					
Parameter	Unit	Value			
Operating Frequency	MHz	440			
Spacecraft Transmit Power	Watts	1.5			
Desired system data rate	bps	57600			
Modulation Method	N/A	QPSK (9.6)			
Hardware/ Environment Parameters					
Spacecraft Antenna Gain	dBi	2.2			
Ground Station Antenna Gain	dBi	14.1			
Spacecraft Transmission Line Losses	dB	2.2			
Spacecraft Antenna Pointing Loss	dB	0.3			
Ground station antenna pointing loss	dB	0.2			
S.C.-to-Gnd Antenna Polarization Loss	dB	0.2			
Ground Station Transmission Line Loss	dB	2.0			
Ground Station Effective Noise Temp	K	509.9			
Ionospheric Loss	dB	0.4			
Eb/ No Threshold	dB	11.6			
Calculated Output Parameters					
Elevation angle [δ]	Degrees	15	25	45	65
Slant Range [S]	km	1,689.6	1,266.7	854.1	688.5
Path Loss	dB	149.9	147.4	144.0	142.1
Atmospheric Losses due to gases	dB	1.1	1.1	0.3	0.3
Total RF power to satellite antenna	dBW	-0.4			
Spacecraft ERIP	dBW	1.7			
Isotropic Signal Level at Ground Station	dBW	-150.2	-147.7	-143.5	-141.6
Ground Station Figure of Merit (G/T)	dB/K	-15.0			
G.S. Signal to Noise Power Density (S/ No)	dBHz	63.2	65.7	70.0	71.8
Telemetary System Eb/ No for downlink	dB	15.6	18.1	22.4	24.2
System Link Margin	dB	4.0	6.5	10.8	12.6

UHF Uplink Budget (EbNo Method)					
Software/ Configuration Parameters					
Parameter	Unit	Value			
Operating Frequency	MHz	430			
Ground Station Transmit Power	Watts	1			
Desired system data rate	bps	57600			
Modulation Method	N/A	QPSK (9.6)			
Hardware/ Environment Parameters					
Spacecraft Antenna Gain	dBi	2.2			
Ground Station Antenna Gain	dBi	16.3			
Spacecraft Receive Line Losses	dB	2.0			
Spacecraft Antenna Pointing Loss	dB	0.6			
Ground station Antenna Pointing Loss	dB	0.3			
Gnd-to-S.C. Antenna Polarization Loss	dB	0.2			
Ground Station Transmission Line Loss	dB	3.6			
Spacecraft Effective Noise Temp	K	261.0			
Ionospheric Loss	dB	0.4			
Eb/ No Threshold	dB	11.6			
Calculated Output Parameters					
Elevation angle [δ]	Degrees	15	25	45	65
Slant Range [S]	km	1,689.6	1,266.7	854.1	688.5
Path Loss	dB	149.7	147.2	143.8	141.9
Atmospheric Losses due to gases	dB	1.1	1.1	0.3	0.3
Total RF power to G.S. antenna	dBW	-3.6			
Ground Station ERIP	dBW	12.7			
Isotropic Signal Level at Spacecraft	dBW	-139.0	-136.5	-132.3	-130.4
Spacecraft Figure of Merit (G/T)	dB/K	-24.0			
S.C. Signal to Noise Power Density (S/ No)	dBHz	65.0	67.5	71.8	73.6
Command System Eb/ No	dB	17.4	19.9	24.1	26.0
System Link Margin	dB	5.8	8.3	12.5	14.4

Figure A.13: Uplink and Downlink budgets for UHF using typical parameters

[1] N. R. C. of the National Academies, Vision and Voyages for Planetary Science in the Decade 2013-2022, The National Academies Press, Washington, D.C., 2011.

[2] H. Yano, T. Kubota, H. Miyamoto, T. Okada, D. Scheeres, Y. Takagi, K. Yoshida, M. Abe, S. Abe, O. Barnouin-Jha, A. Fujiwara, S. Hasegawa, T. Hashimoto, M. Ishiguro, M. Kato, J. Kawaguchi, T. Mukai, J. Saito, S. Sasaki, M. Yoshikawa, Touchdown of the Hayabusa Spacecraft at the Muses Sea on Itokawa, Science 312 (2006) 1350–1353.

[3] E. Hand, Philae probe makes bumpy touchdown on a comet, Science 346 (2014) 900–901.

[4] R. Z. Sagdeev, A. V. Zakharov, Brief history of the Phobos mission, Nature 341 (1989) 581–585.

[5] L. R. Nittler, Near-Shoemaker at Eros: The first detailed exploration of an asteroid, Elements 10 (2014) 51–52.

[6] T. Saiki, H. Sawada, C. Okamoto, H. Yano, Y. Takagi, Y. Akahoshi,

S-Band Downlink Budget (EbNo Method)

Software/ Configuration Parameters

Parameter	Unit	Value			
Operating Frequency	MHz	1610			
Spacecraft Transmit Power	Watts	10			
Desired system data rate	bps	115200			
Modulation Method	N/A	BPSK (9.6)			

Hardware/ Environment Paramters

Parameter	Unit	Value			
Spacecraft Antenna Gain	dBi	6.0			
Ground Station Antenna Gain	dBi	28.3			
Spacecraft Transmission Line Losses	dB	2.2			
Spacecraft Antenna Pointing Loss	dB	0.6			
Ground station antenna pointing loss	dB	8.0			
S.C.-to-Gnd Antenna Polarization Loss	dB	0.2			
Ground Station Receive Line Loss	dB	2.0			
Ground Station Effective Noise Temp	K	509.9			
Ionospheric Loss	dB	0.8			
Eb/ No Threshold	dB	11.6			

Calculated Output Parameters

Parameter	Unit				
Elevation angle [δ]	Degrees	15	25	45	65
Slant Range [S]	km	1,689.6	1,266.7	854.1	688.5
Path Loss	dB	161.2	158.7	155.2	153.4
Atmospheric Losses due to gases	dB	1.1	1.1	0.3	0.3
Total RF power to satellite antenna	dBW	7.8			
Spacecraft ERIP	dBW	13.8			
Isotropic Signal Level at Ground Station	dBW	-150.0	-147.5	-143.3	-141.4
Ground Station Figure of Merit (G/T)	dB/K	-0.7			
G.S. Signal to Noise Power Density (S/ No)	dBHz	69.8	72.3	76.5	78.4
Telemetary System Eb/ No for downlink	dB	19.2	21.7	25.9	27.8
System Link Margin	dB	7.6	10.1	14.3	16.2

S-Band Uplink Budget (EbNo Method)

Software/ Configuration Parameters

Parameter	Unit	Value			
Operating Frequency	MHz	1620			
Ground Station Transmit Power	Watts	10			
Desired system data rate	bps	115200			
Modulation Method	N/A	BPSK (9.6)			

Hardware/ Environment Paramters

Parameter	Unit	Value			
Spacecraft Antenna Gain	dBi	6.0			
Ground Station Antenna Gain	dBi	36.6			
Spacecraft Receive Line Losses	dB	2.0			
Spacecraft Antenna Pointing Loss	dB	0.6			
Ground station Antenna Pointing Loss	dB	21.9			
Gnd-to-S.C. Antenna Polarization Loss	dB	0.2			
Ground Station Transmission Line Loss	dB	3.6			
Spacecraft Effective Noise Temp	K	261.0			
Ionospheric Loss	dB	0.4			
Eb/ No Threshold	dB	11.6			

Calculated Output Parameters

Parameter	Unit				
Elevation angle [δ]	Degrees	15	25	45	65
Slant Range [S]	km	1,689.6	1,266.7	854.1	688.5
Path Loss	dB	161.2	158.7	155.3	153.4
Atmospheric Losses due to gases	dB	1.1	1.1	0.3	0.3
Total RF power to G.S. antenna	dBW	6.4			
Ground Station ERIP	dBW	43.0			
Isotropic Signal Level at Spacecraft	dBW	-141.8	-139.3	-135.1	-133.2
Spacecraft Figure of Merit (G/T)	dB/K	-20.1			
S.C. Signal to Noise Power Density (S/ No)	dBHz	66.1	68.6	72.8	74.7
Command System Eb/ No	dB	15.5	18.0	22.2	24.1
System Link Margin	dB	3.9	6.4	10.6	12.5

Figure A.14: Uplink and Downlink budgets for S-Band using typical parameters

M. Yoshikawa, Small carry-on impactor of Hayabusa2 mission, Acta Astronautica 84 (2013) 227–236.

[7] C. Lange, C. Dietze, T.-M. Ho, O. Kroemer, M. Lange, S. Wagenbach, L. Witte, The MASCOT-Study Team, Baseline Design of a Mobile Asteroid Surface Scout (MASCOT) for the Hayabusa 2 Mission.

[8] T. Yoshimitsu, T. Kubota, A. Tomiki, MINERVA-II rovers developed for Hayabusa-2 mission, in: Low Cost Planetary Missions Conference-11, June, 2015.

[9] K. Ennico, D. Durda, Box of Rocks: An experiment to study the evolution of regolith blocks in microgravity, in: Next-Generation Suborbital Researchers Conference, 2011.

[10] F. J. Haddy, NASA has its biological groundwork for a trip to Mars improved?, The FASEB Journal 21 (2007) 643–646.

[11] T. Taylor, Centrifugal gravity habitation torus constructed of salvaged orbital debris, 2001. US Patent 6,206,328.

[12] G. H. Fichtl, R. L. Holland, Simplified model of statistically stationary spacecraft rotation and associated induced gravity environments, NASA-TM-78164, 1978.

[13] E. Asphaug, J. Thangavelautham, Asteroid Regolith Mechanics and Primary Accretion Experiments in a Cubesat, in: Proceedings of the 45th Lunar and Planetary Science Conference, Houston, Texas, March, 2014, Paper 2306.

[14] J. Thangavelautham, A. Thoesen, F. Gadau, G. Hutchins, E. Asphaug, I. Alizadeh, Low-Cost Science Laboratory in Microgravity Using a CubeSat Centrifuge Framework, in: Proceedings of the 65th International Astronautical Congress, Toronto, 2014.

[15] A. Johansen, E. Jacquet, J. N. Cuzzi, A. Morbidelli, M. Gounelle, New Paradigms For Asteroid Formation, in: Asteroids IV, University of Arizona Press, 2015, pp. 471–492.

[16] J. Brisset, D. Heißelmann, S. Kothe, R. Weidling, J. Blum, The Suborbital Particle Aggregation and Collision Experiment (SPACE): Studying the collision behavior of submillimeter-sized dust aggregates on the suborbital rocket flight REXUS 12, Review of Scientific Instruments 84 (2013) 094501.

[17] S. G. Love, D. R. Pettit, S. R. Messenger, Particle aggregation in microgravity: Informal experiments on the International Space Station, Meteoritics & Planetary Science 49 (2014) 732–739.

[18] J. R. Marshall, T. B. Sauke, J. N. Cuzzi, Microgravity studies of aggregation in particulate clouds, Geophysical Research Letters 32 (2005) 11202.

[19] G. Praburam, J. Goree, Cosmic dust synthesis by accretion and coagulation, Astrophysical Journal 441 (1995) 830–838.

[20] H. Chennaoui-Aoudjehane, A. Jambon, M. Bourot Denise, O. Boudouma, J. Gattacceca, P. Weber, P. Bonté, Tamdakht Meteorite: The last Moroccan fall, Meteoritics and Planetary Science Supplement 72 (2009) 5038.

[21] K. E. Tsiolkovsky, Grezy O Zemle I Nebe [i] Na Vests (Speculations of Earth and Sky, and On Vesta, science fiction works), Izd-vo AN SSR, 1895.

[22] T. W. Hall, The Architecture of Artificial-Gravity Environments for Long-Duration Space Habitation (University Microfilms 9423117), Doctoral dissertation, University of Michigan, 1994.

[23] K. Gatland, Manned Spacecraft, MacMillan Publishing Co., Inc., second edition, 1976.

[24] K. Kumar, Review on dynamics and control of nonelectrodynamic tethered satellite systems, Journal of Spacecraft and Rockets 43 (2006) 705–720.

[25] M. P. Cartmell, D. J. McKenzie, A review of space tether research, Progress in Aerospace Sciences 44 (2008) 1–21.

[26] A. K. Misra, Dynamics and control of tethered satellite systems, Acta Astronautica 63 (2008) 1169–1177.

[27] Z. Cai, X. Li, H. Zhou, Nonlinear dynamics of a rotating triangular tethered satellite formation near libration points, Aerospace Science and Technology 42 (2015) 384 – 391.

[28] B. Wong, A. Misra, Planar dynamics of variable length multi-tethered spacecraft near collinear Lagrangian points, Acta Astronautica 63 (2008) 1178–1187.

[29] B. Dalton, K. Plaut, G. Meeker, Life sciences research in the Centrifuge Accommodation Module of the International Space Station, Technical Report 2000-01-2247, SAE, 2000.

[30] H. Gindl, J. Scheimann, M. Shirakawa, V. Suvorov, J. Uri, Research on International Space Station - Building a Partnership for the Future, in: 55th International Astronautical Congress, Vancouver, 2004.

[31] M. Holderman, E. Henderson, Nautilus-X multi-mission space exploration vehicle, Future in Space Operations (FISO) Colloquium, 2011.

[32] J. Z. Kiss, Plant biology in reduced gravity on the Moon and Mars, Plant Biology 16 (2014) 12–17.

[33] D. Cotto-Figueroa, E. Asphaug, L. A. J. Garvie, A. Rai, J. Johnston, L. Borkowski, S. Datta, A. Chattopadhyay, M. A. Morris, Scale-dependent measurements of meteorite strength: Implications for asteroid fragmentation, Icarus 277 (2016) 73–77.

[34] CubeSat Design Specification (CDS) - Rev. 13, April, 2015.

[35] B. D. Lucas, T. Kanade, An Iterative Image Registration Technique with an Application to Stereo Vision (DARPA), in: Proceedings of the 1981 DARPA Image Understanding Workshop, 1981, pp. 121–130.

[36] B. K. Horn, B. G. Schunck, Determining optical flow, Artificial Intelligence 17 (1981) 185–203.

[37] J. Thangavelautham, T. Barfoot, G. D'Eleuterio, Coevolving Communication and Cooperation for Lattice Formation Tasks (Updated), in: Advances In Artificial Life: Proc. of the 7th European Conference on ALife (ECAL), Springer-Verlag, 2003, pp. 857–864.

[38] J. Thangavelautham, T. Barfoot, G. D'Eleuterio, Evolutionary-Based Control Approaches for Multirobot Systems, in: Frontiers in Evolutionary Robotics, Intech, 2008, pp. 35–60.

[39] V. Perera, N. Movshovitz, E. Asphaug, J. Thangavelautham, Material Studies of Asteroid Regolith and Accretion Using a Low-Cost CubeSat Laboratory, in: Proceedings of the 65th International Astronautical Congress, Toronto, 2014.